

Three-Dimensional Magnetization-Prepared Imaging Using a Concentric Cylinders Trajectory

Kie Tae Kwon,^{1*} Holden H. Wu,^{1–3} Taehoon Shin,¹ Tolga Çukur,⁴ Michael Lustig,⁵ and Dwight G. Nishimura¹

Purpose: To develop new magnetization-prepared imaging schemes based on a three-dimensional (3D) concentric cylinders trajectory.

Methods: The 3D concentric cylinders trajectory, which is robust to off-resonance effects and timing delays while requiring fewer excitations than a comparable 3D Cartesian (3DFT) sequence, is used as the readout for magnetization-prepared sequences exploiting its inherently centric-ordered structure. Two applications: (i) T_1 -weighted brain imaging with an inversion-recovery-prepared radiofrequency-spoiled gradient-echo (IR-SPGR) sequence, (ii) non-contrast-enhanced (NCE) peripheral angiography with a magnetization-prepared balanced steady-state free precession (bSSFP) sequence are presented to demonstrate the effectiveness of the proposed method. For peripheral angiography, the scan efficiency is further improved by interleaving different preparations at different rates and by carefully designing the sampling geometry for an efficient parallel imaging method.

Results: In vivo brain scans with an IR-SPGR sequence and lower extremity scans with a magnetization-prepared bSSFP sequence for NCE peripheral angiography both demonstrate that the proposed sequences with concentric cylinders effectively capture the transient magnetization-prepared contrast with faster scan times than a corresponding 3DFT sequence. The application of peripheral angiography also shows the feasibility of the proposed interleaving schemes and parallel imaging method.

Conclusion: The 3D concentric cylinders trajectory is a robust and efficient readout that is well-suited for magnetization-prepared imaging. *Magn Reson Med* 71:1700–1710, 2014. © 2013 Wiley Periodicals, Inc.

Key words: non-Cartesian trajectories; 3D concentric cylinders; magnetization-prepared imaging

INTRODUCTION

Magnetization-prepared imaging is a widely used technique to improve the intrinsic contrast in MR images. It uses a set of magnetization preparations to generate a desired, albeit transient, contrast. Depending on the application, various preparations can be used such as inversion recovery for T_1 contrast (1–4), T_2 -preparation for T_2 contrast (5), fat saturation for water-fat contrast (6,7), or venous saturation for artery-vein contrast (8). A separate readout is then used to capture the contrast generated by these preparations. Because most of the energy of an MR image is concentrated at low spatial frequencies, the readout typically uses centric view ordering (9,10) to effectively capture the transient magnetization-prepared contrast. In addition, k-space segmentation (11,12) is used to mitigate k-space weighting that otherwise may cause artifacts such as spatial blurring. In this manner, the quality of the acquired image is intricately tied to the effectiveness and robustness of the k-space sampling trajectory used during the readout.

Both Cartesian and non-Cartesian trajectories have been previously used for magnetization-prepared imaging (13–16). Cartesian trajectories offer improved immunity against hardware imperfections, but suffer from prolonged scan times due to the larger number of excitations required. On the other hand, although most non-Cartesian trajectories yield improved scan efficiency, they are more susceptible to off-resonance effects and gradient timing delays. In contrast, a three-dimensional (3D) concentric cylinders trajectory (17–21) is a hybrid that offers a favorable balance between Cartesian and non-Cartesian sampling properties. Previously, the trajectory was incorporated into T_1 and T_2 -weighted Carr–Purcell–Meiboom–Gill spin-echo-train sequences (18,19) and a general purpose 3D gradient-recalled echo pulse sequence (20,21). While requiring fewer excitations and thus shorter scan times than a comparable 3D Cartesian (3DFT) sequence, concentric cylinders also exhibit more robustness to off-resonance effects (21) and timing delays (22) compared to other non-Cartesian trajectories. In addition, the view ordering of concentric cylinders is inherently centric-ordered in two dimensions and is capable of smooth k-space weighting with segmentation. Thus, the concentric cylinders trajectory is a promising candidate for magnetization-prepared imaging.

In this work, new magnetization-prepared imaging schemes based on the 3D concentric cylinders trajectory are developed. Two applications: (i) T_1 -weighted brain imaging with an inversion-recovery-prepared (IR) radiofrequency (RF)-spoiled gradient-echo (SPGR) sequence, (ii) non-contrast-enhanced (NCE) peripheral angiography with

¹Department of Electrical Engineering, Magnetic Resonance Systems Research Laboratory, Stanford University, Stanford, California, USA.

²Division of Cardiovascular Medicine, Stanford University, Stanford, California, USA.

³Department of Radiological Sciences, University of California at Los Angeles, Los Angeles, California, USA.

⁴Helen Wills Neuroscience Institute, University of California at Berkeley, Berkeley, California, USA.

⁵Department of Electrical Engineering and Computer Science, University of California at Berkeley, Berkeley, California, USA.

Grant sponsor: National Institutes of Health and GE Healthcare; Grant numbers: R01 HL075803, R01 HL039297; Grant sponsor: Samsung Scholarship (K.T.K)

*Correspondence to: Kie Tae Kwon, M.S., Packard Electrical Engineering, Room 208, 350 Serra Mall, Stanford, CA 94305-9510. E-mail: ktkwon07@stanford.edu

Received 28 January 2013; revised 15 April 2013; accepted 30 April 2013.

DOI 10.1002/mrm.24823

Published online 1 July 2013 in Wiley Online Library (wileyonlinelibrary.com).

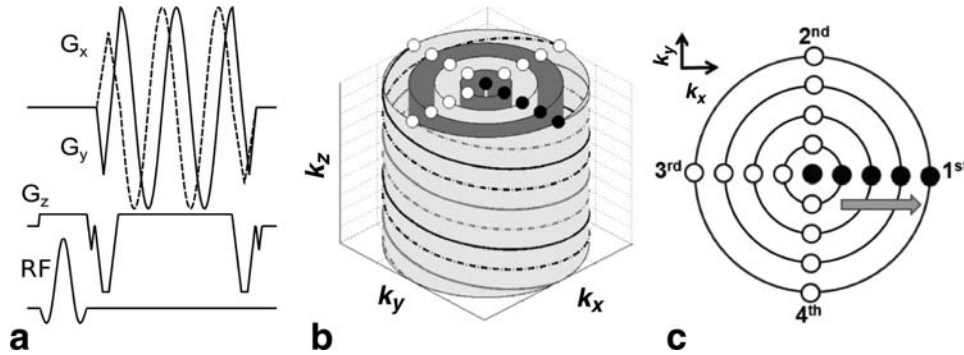


FIG. 1. 3D concentric cylinders trajectory. Pulse sequence timing diagram (a) and corresponding k-space trajectory (b) with $N_{cy} = 5$ cylinders (the radius of the innermost cylinder is 0). $N_{intlv} = 4$ helical interleaves with $N_{rev} = 2$ revolutions are shown on the side of the outermost cylinder. Dots represent end points of interleaves. c: Centric view ordering with $N_{seg} = 4$ segments viewed from the k_z axis. The collection of black dots represents the first segment and the arrow shows the center-out acquisition direction for the first segment, which yields smooth k-space weighting.

a magnetization-prepared balanced steady-state free precession (bSSFP) sequence are presented to demonstrate the effectiveness of the proposed method. For peripheral angiography, the scan efficiency is further improved by interleaving different preparations at different rates and by carefully designing the sampling geometry for an efficient parallel imaging method. For both in vivo applications, data from healthy volunteers demonstrate that the proposed sequences with concentric cylinders effectively capture the transient magnetization-prepared contrast with faster scan times than a corresponding 3DFT sequence. The application of peripheral angiography also shows the feasibility of the proposed interleaving schemes and parallel imaging method.

METHODS

3D Concentric Cylinders Trajectory

The 3D concentric cylinders trajectory we have implemented derives from a 2D concentric rings trajectory (23) by adding a constant G_z gradient to oscillating G_x and G_y gradients during the readout (Fig. 1a). Similar to the 2D concentric rings trajectory, G_x and G_y gradients are designed for the outermost cylinder and then scaled down for the inner cylinders, with the readout duration kept constant. Meanwhile, each of N_{cy} uniformly spaced concentric cylinders is covered by a set of N_{intlv} uniformly distributed helical interleaves with N_{rev} revolutions (Fig. 1b). N_{cy} determines the in-plane (x - y) field of view (FOV), whereas N_{intlv} and N_{rev} determine the through-plane (z) FOV once the radius and height of the outermost cylinder are set from the desired spatial resolution. The matrix size of the reconstructed image after 3D gridding is $2N_{cy} \times 2N_{cy} \times N_{slice}$, where $N_{slice} = N_{intlv} \cdot N_{rev}$. N_{rev} should be chosen as a trade-off between the total number of excitations ($N_{cy} \cdot N_{intlv}$) and the readout duration per interleaf (T_{read}). This sequence approximately requires a factor of $2N_{rev}$ fewer excitations than a comparable 3DFT sequence, but the readout duration ($\propto N_{rev}$) also needs to be within a reasonable range depending on the application.

The scale-down and interleaved design of concentric cylinders does not fully exploit the maximum gradient amplitude and slew rate for the inner cylinders, but it ensures the following unique properties. First, the constant G_z gradient converts the off-resonance behavior from a blur (typical of non-Cartesian trajectories) into a benign geometric shift in the z -direction (21). The amount of shift in the constant readout direction for an off-resonance frequency (Δf) is approximately $T_{read} \cdot \Delta f$ voxels as in the case of 3DFT. Second, the effect of gradient timing delays (τ) manifests as a bulk in-plane rotation in the reconstructed magnitude image because the entire set of k-space samples is rigidly rotated in the k_x - k_y plane (22). The amount of rotation in the x - y plane is $360 \cdot N_{rev} \cdot \tau / T_{read}$ degrees, which is the same as that in the k_x - k_y plane.

Parallel Imaging with Cylinders

With the scale-down and interleaved design, the sampling geometry of concentric cylinders can be designed in a way that the original 3D non-Cartesian data are reformatted as a set of 2D Cartesian spoke-planes (24), which cut through the cylinders along full-diameter spokes (Fig. 2a and b). This reformatting is possible if the following two conditions are met: (i) $N_{intlv} = \text{even number}$, (ii) N_{samp} (the number of sampling points per interleaf) = integer multiple of N_{slice} . The first condition can be easily met, and the second condition can be satisfied by adjusting the in-plane FOV and the sampling rate for a given N_{slice} . Although spoke-planes are slightly shifted with respect to each other in the k_z -direction due to the constant G_z gradient, data points in each spoke-plane remain on a 2D Cartesian grid (Fig. 2c), and the maximum shift between different spoke-planes (w in Fig. 2 a) is less than $1/N_{slice}$ of the maximum k_z extent. Thus, it is possible to apply a k-space-based 2D Cartesian parallel imaging reconstruction for each spoke-plane.

Undersampling is achieved by acquiring interleaves fewer than the N_{intlv} necessary for full-FOV in the z -direction. Figure 2d shows a uniform undersampling pattern with a reduction factor $R = 2$, which corresponds to acquiring even-numbered interleaves for odd-numbered

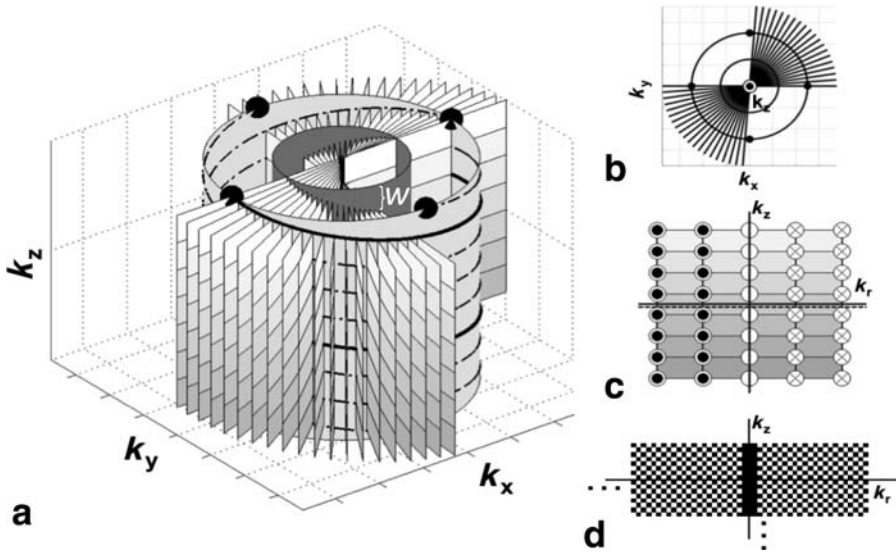


FIG. 2. Parallel imaging with concentric cylinders. **a**: k -space trajectory of concentric cylinders with $N_{cy} = 3$, $N_{intlv} = 4$, $N_{rev} = 2$, $N_{slice} = 8$, and $N_{samp} = 160$. Depicted are 20 of a total of 40 full-diameter spoke-planes, which are slightly shifted in the k_z direction (w : the maximum shift). **b**: View from the k_z axis. **c**: View of a spoke-plane with data points on a 2D Cartesian grid (k_r : the radial axis of each spoke-plane, which is slightly shifted from $k_z = 0$ (dashed line). Left side: interleaves coming out, right side: going in). **d**: Uniform undersampling pattern ($R = 2$) with fully sampled center (black: sampled, white: unsampled) for autocalibration.

cylinders and vice versa. Interleaves of certain numbers of inner cylinders are fully acquired for autocalibration. After missing points in each spoke-plane are filled using a k -space-based 2D Cartesian parallel imaging reconstruction, 3D gridding reconstruction is performed for each coil as a regular fully acquired case.

Magnetization-Prepared Imaging with Cylinders

Concentric cylinders are well-suited for magnetization-prepared imaging due to the inherent centric view ordering in the k_x and k_y dimensions along with the aforementioned properties. Once divided into several segments (N_{seg}), each segment can be collected in a centric-ordered manner to effectively capture the transient contrast created by magnetization preparation. Figure 1c shows a simple example of view ordering with $N_{seg} = N_{intlv}$, where helical interleaves at the same angular location are collected together starting from the innermost cylinder for each segment. The view ordering of N_{seg} segments to acquire a total of $N_{cy} \cdot N_{intlv}$ helical interleaves depends on the application, but in general, concentric cylinders provide smooth k -space weighting and capture the contrast more compactly than a regular 1D centric-ordered 3DFT sequence.

Inversion-Recovery-Prepared Brain Imaging with Cylinders

T_1 -weighted brain imaging with an IR-SPGR sequence (1) is considered as the first application to demonstrate the effectiveness of concentric cylinders for 3D magnetization-prepared imaging. Figure 3a shows the overall pulse sequence diagram we have implemented. First, an adiabatic inversion pulse (25) with a subsequent inversion time (TI) is played to achieve white matter-gray matter (WM-GM) contrast. This is followed by a dummy readout and a segment of concentric cylinders readout with durations T_{dummy} and T_{acqwnd} , respectively. Finally, a recovery time (TD) is applied before the next repetition. This full cycle is repeated $N_{seg} + 2$ times, where the first two repetitions without data acquisition were used to stabilize the evolution of signal (22).

For in vivo brain scans, TI/TD = 600/0 ms (scheme A) and 900/600 ms (scheme B) were used, which were adapted from Wu et al. (22). The other sequence parameters were isotropic spatial resolution = 1.1 mm, FOV = $31.7 \times 31.7 \times 19.8 \text{ cm}^3$, echo time (TE)/pulse repetition time (TR) = 6.5/15.6 ms, flip angle = 15° , $T_{dummy} = 78 \text{ ms}$ (5 TRs), $T_{acqwnd} = 1123 \text{ ms}$ (72 TRs), and readout bandwidth = $\pm 125 \text{ kHz}$ ($4 \mu\text{s}/\text{sample}$). Concentric cylinders were implemented with $N_{cy} = 144$, $N_{slice} = 180$, $N_{intlv} = 60$, $N_{rev} = 3$, $N_{samp} = 2712$ (10.85 ms), and $N_{seg} = 120$ to divide each set of helical interleaves at the same angular location into two segments (72 encodings per segment).

NCE Magnetization-Prepared bSSFP Peripheral Angiography with Cylinders

As the second application, NCE peripheral angiography with a magnetization-prepared bSSFP sequence is considered. (26–28). Concentric cylinders can be easily used for a bSSFP sequence due to its inherently balanced gradient waveforms. However, the view ordering needs to be carefully decided to prevent eddy currents from degrading the quality of the bSSFP images (29), and a “pairing” strategy (Fig. 4a) can be applied to stabilize the otherwise disturbed magnetization produced by the changing gradients (30).

Figure 3b shows the overall pulse sequence diagram we have implemented, which starts with a set of magnetization preparations. First, an adiabatic inversion pulse (25) with a subsequent TI is played to suppress long- T_1 fluids such as joint fluid or edema, which can otherwise hinder the depiction of arterial blood in the bSSFP images due to their higher T_2/T_1 ratios. Next, an adiabatic B_1 -insensitive rotation (BIR-4) pulse (31) for T_2 -preparation is played to create T_2 -dependent artery-vein contrast (due to the lower T_2 of deoxygenated venous blood) and artery-muscle contrast. Following the T_2 -preparation, a venous saturation pulse is played to saturate a region inferior to the FOV to help suppress venous blood flowing into the FOV. Because of slow venous flow, this venous suppression scheme necessitates a thin-slab-scan approach (32)

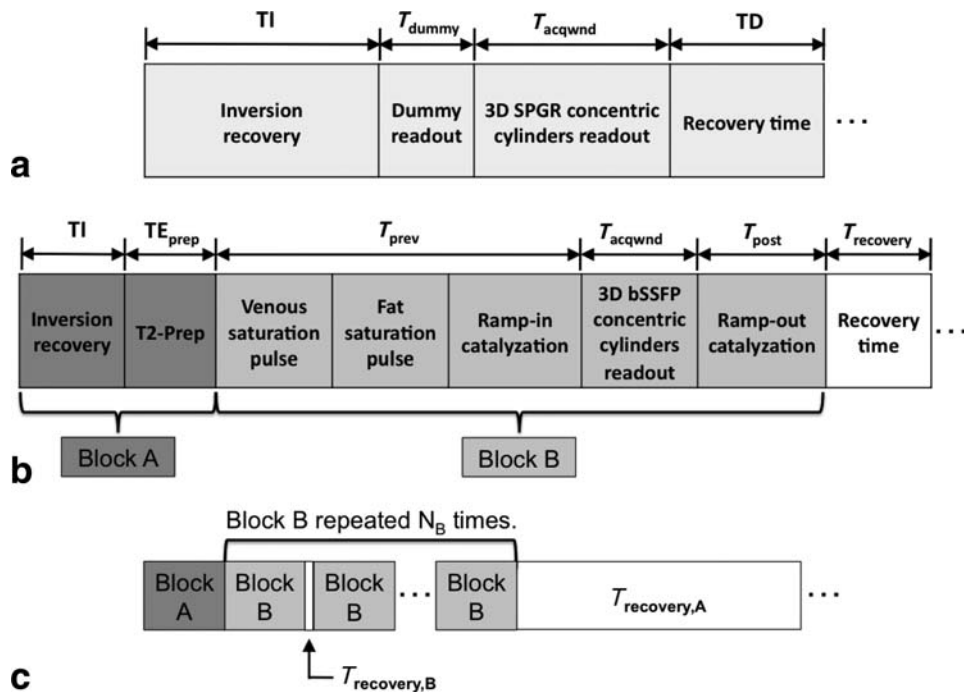


FIG. 3. **a**: Pulse sequence diagram of an IR-SPGR sequence for T_1 -weighted brain imaging. **b**: Pulse sequence diagram of a magnetization-prepared bSSFP sequence for peripheral angiography. **c**: Acquisition strategy with repetitions of preparations at different rates. The inversion recovery and the T_2 -preparation (block A) are repeated once for every N_B repetitions of the venous/fat saturation pulses and the readout components (block B) to improve the scan efficiency.

for volumetric coverage. Finally, a fat saturation pulse is played right before a bSSFP raised cosine-windowed ramp-in catalyztion. The transient contrast generated by these preparations is then captured by a segment of concentric cylinders readout, which is followed by a ramp-out catalyztion and a recovery time.

Sequence Design for Peripheral Angiography: Magnetization Preparation

The relaxation parameters (T_1/T_2) of the tissues targeted by the aforementioned magnetization preparations are approximately 2850/1210 ms for joint fluid, 1273/254 ms for arterial blood, 1273/159 ms for venous blood, 260/80

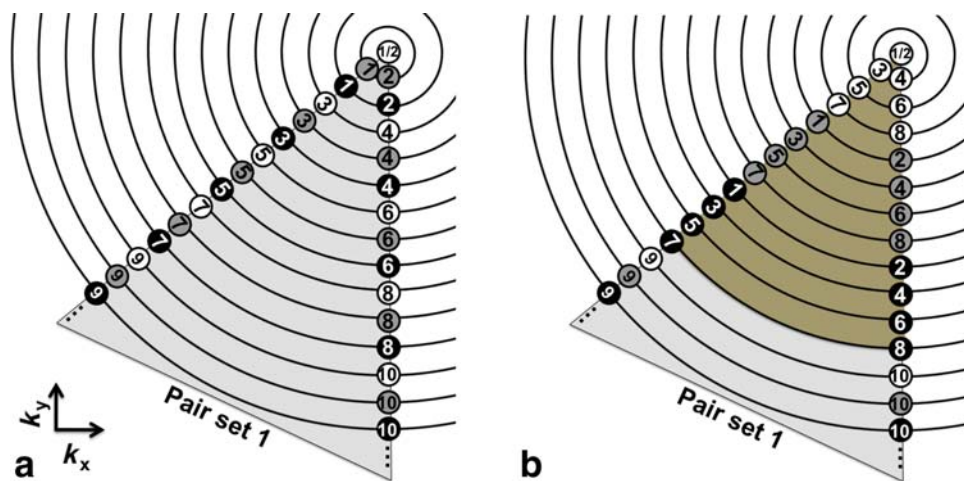


FIG. 4. View ordering of concentric cylinders for a magnetization-prepared bSSFP sequence (view from the k_z axis). Small dots represent starting points of helical interleaves, which are divided into three segments (white, gray, and black) that are collected sequentially with orders shown on dots (total 10 dots per each segment). Adjacent interleaves on each cylinder are collected as a pair to stabilize the otherwise disturbed magnetization produced by the changing gradients. One way of view ordering is to be solely based on interleaved segmentation in the radial direction (**a**), but another way is to be based on a mixture of sequential (e.g., the first 12 cylinders highlighted with a darker background) and interleaved segmentation (**b**). [Color figure can be viewed in the online issue, which is available at wileyonlinelibrary.com.]

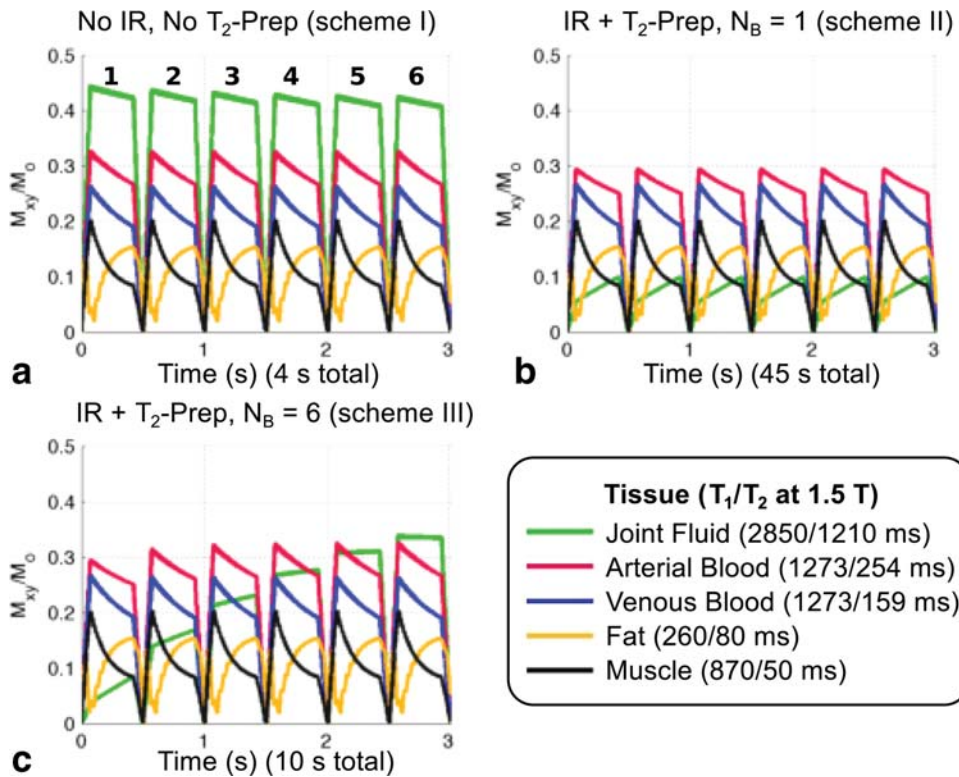


FIG. 5. Bloch simulations of magnetization-prepared bSSFP sequences. **a**: Without inversion recovery and T_2 -preparation (scheme I). **b**: With inversion recovery and T_2 -preparation, $N_B = 1$ (scheme II). **c**: With inversion recovery and T_2 -preparation, $N_B = 6$ (scheme III). Six segments are shown for each scheme. Scheme III (**c**) provides a flexible trade-off between fluid suppression and scan time, with comparable blood-muscle contrast to schemes I and II.

ms for fat, and 870/50 ms for muscle at 1.5 T (33–35). Due to their wide ranges, the sequence is required to have both a short acquisition window (T_{acqwnd}) and a long recovery time (T_{recovery}) per readout segment. More specifically, T_{recovery} needs to be long enough (few seconds) to allow sufficient recovery of fluid before the next inversion recovery, whereas T_{acqwnd} needs to be short enough (few hundred milliseconds) to avoid too much recovery of venous and fat signals during the readout. These requirements will prolong the scan time as they together need an increased number of k-space segments with a longer recovery time.

To maintain a reasonable scan time, we divide the preparations into two groups, where the inversion recovery and the T_2 -preparation are included in block A, whereas the remaining preparations (venous/fat saturation pulses) are included in block B (Fig. 3b) with the readout components. In addition, we use two different recovery times $T_{\text{recovery},A}$ and $T_{\text{recovery},B}$ for each block, with which blocks A and B are repeated at different rates (Fig. 3c). More specifically, block A and the long $T_{\text{recovery},A}$ for the inversion recovery in block A are repeated only once for every N_B repetitions of block B. With this scheme, T_{acqwnd} can be shortened enough to capture the transient contrast generated by venous and fat saturation pulses, whereas TI and $T_{\text{recovery},A}$ can be repeated less frequently to substantially reduce the scan time asymptotically by a factor of N_B . The T_2 -preparation in block A is dedicated to suppress the almost fully recovered muscle signal during TI, which together with the short $T_{\text{recovery},B}$ provide sufficient artery-muscle contrast.

Figure 5 shows the transient bSSFP signals simulated for three different schemes: (a) without inversion recovery and T_2 -preparation (scheme I), (b) $N_B = 1$ with inversion recovery and T_2 -preparation (scheme II), and (c) $N_B = 6$

with inversion recovery and T_2 -preparation (scheme III, which also generally implies cases with $N_B > 1$). Each scheme was simulated for six segments of bSSFP readout. The preparation and the recovery periods among the segments are not shown on the time axis for ease of comparison among different schemes. However, the actual scan time for each scheme will be different depending on the preparation and the recovery times. In every case, the fat saturation pulse was applied but the venous saturation pulse was not applied to show the effect of the T_2 -preparation on venous blood. Proton densities were assumed to be the same for all the tissues, and tissues other than fat (-220 Hz at 1.5 T) were assumed to be on-resonance. The sequence parameters were flip angle = 70° , TE/TR = 3.4/7.4 ms, TI = 2 s, $TE_{\text{prep}} = 40$ ms, $T_{\text{prep}} = 114$ ms (40 ms + 10 TRs), $T_{\text{acqwnd}} = 355$ ms (48 TRs), $T_{\text{post}} = 74$ ms (10 TRs), $T_{\text{recovery},A} = 5$ s, and $T_{\text{recovery},B} = 200$ ms (Fig. 3b and c). With these parameters, the actual scan time of each scheme for six segments will be 4, 45, and 10 s, respectively. Although scheme II (Fig. 5b) provides the best fluid suppression with a much longer scan time than others, scheme III (Fig. 5c) provides a flexible trade-off between fluid suppression and scan time. With a moderate number of N_B , sufficient fluid suppression can still be achieved. In addition, scheme III provides comparable artery-muscle contrast to schemes I and II, as expected from the short $T_{\text{recovery},B}$ and the T_2 -preparation in block A.

Sequence Design for Peripheral Angiography: Cylinders Readout

For schemes I and II, the signal evolution of each tissue is almost the same across the readout segments. Therefore,

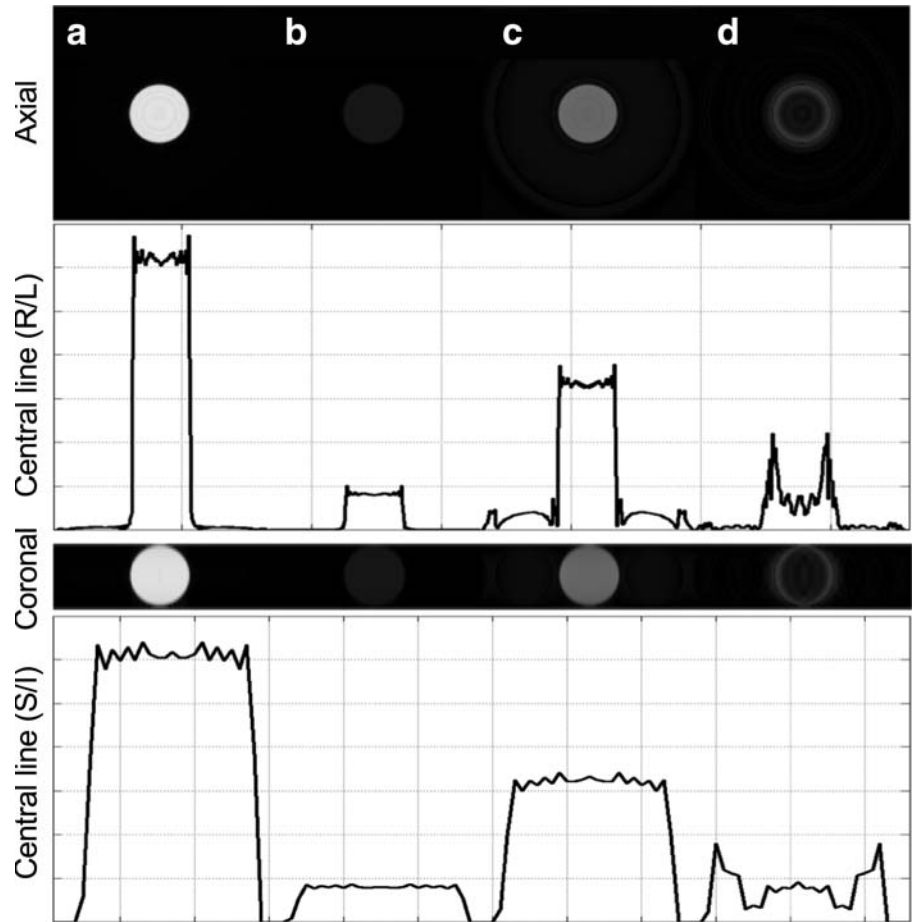


FIG. 6. Simulations of fluid suppression. An axial image with a plot of central line in the R/L direction (top) and a coronal image with a plot of central line in the S/I direction (bottom) of a 3D analytical sphere phantom are shown for different schemes. Scheme II (b) reduces the amplitude of the phantom down to 13 % of scheme I (a), but it requires a relatively long scan time. For scheme III with $N_B = 6$, scheme III-int (c) with interleaved segmentation reduces the amplitude down to 53% of scheme I, but it is with relatively large sidelobes in the axial plane. In contrast, scheme III-mix (d) with a mixture of sequential and interleaved segmentation reduces the amplitude down to 35% of scheme I, and is with much reduced sidelobes in the axial plane.

regular interleaved segmentation with centric view ordering is used to collect the encodings (helical interleaves) of concentric cylinders. Figure 4a illustrates an example where a set consisting of pairs of encodings is divided into three interleaved segments, which are on cylinders with index $[1, 4, 7, 10, 13, \dots]$, $[2, 5, 8, 11, 14, \dots]$, and $[3, 6, 9, 12, 15, \dots]$ (the index starts from 1, indicating the innermost cylinder with radius 0). These are repeated for other sets, and in this example, a total of $N_{\text{seg}} = 3 \cdot (N_{\text{intlv}}/2)$ segments would be needed.

Unlike schemes I and II, scheme III exhibits a relatively strong variation of fluid signal evolution across the readout segments. The variation is periodic with a period of N_B readout segments, and the intended contrast is achieved more at the beginning of each period. The regular interleaved segmentation can still be used for scheme III (scheme III-int), but the periodic variation may necessitate a mixture of sequential and interleaved segmentation (scheme III-mix). In both cases, the number of segments for each set of pairs needs to be an integer multiple of N_B to avoid any variation of k-space weighting of fluid across the sets. Figure 4b illustrates an example when $N_B = 3$, where the three hybrid segments of a set are on cylinders with index $[1, 2, 3, 4, 13, \dots]$, $[5, 6, 7, 8, 14, \dots]$, and $[9, 10, 11, 12, 15, \dots]$. The sequential portion (the first four indices) helps achieve more smooth and suppressed weighting for fluid in the center of k-space, whereas the remaining interleaved

portion maintains smooth weighting for the other four tissues. Therefore, the segmentation needs to be chosen in a balanced manner.

Figure 6 shows the degree of fluid suppression of different schemes simulated with a 3D analytical sphere phantom (36). Concentric cylinders were used as the readout trajectory and were implemented with $N_{\text{cy}} = 144$, $N_{\text{slice}} = 24$, $N_{\text{intlv}} = 12$, $N_{\text{rev}} = 2$, $N_{\text{samp}} = 864$ (3.4 ms), and $N_{\text{seg}} = 36$ to divide each set of pairs into six segments (48 encodings per segment). Additional sequence parameters were spatial resolution = $1.1 \times 1.1 \times 2.2 \text{ mm}^3$ (in the order of A/P, R/L, and S/I directions), FOV = $31.7 \times 31.7 \times 5.3 \text{ cm}^3$, and readout bandwidth = $\pm 125 \text{ kHz}$ ($4 \mu\text{s}/\text{sample}$). Scheme II (Fig. 6b) reduces the amplitude of the phantom down to 13 % of scheme I (Fig. 6a), which is the largest reduction as expected. For scheme III with $N_B = 6$, scheme III-int (Fig. 6c) with interleaved segmentation reduces the amplitude down to 53% of scheme I, but it is with relatively large sidelobes in the plane. In contrast, scheme III-mix (Fig. 6d) with a mixture of sequential (the first 12 encodings) and interleaved (the remaining 36 encodings) segmentation reduces the amplitude down to 35% of scheme I, and comes with much reduced sidelobes in the axial plane. However, the peak amplitude is prominently localized around the edge with high spatial frequencies, which is probably because scheme III-mix focuses much more on suppressing the center of

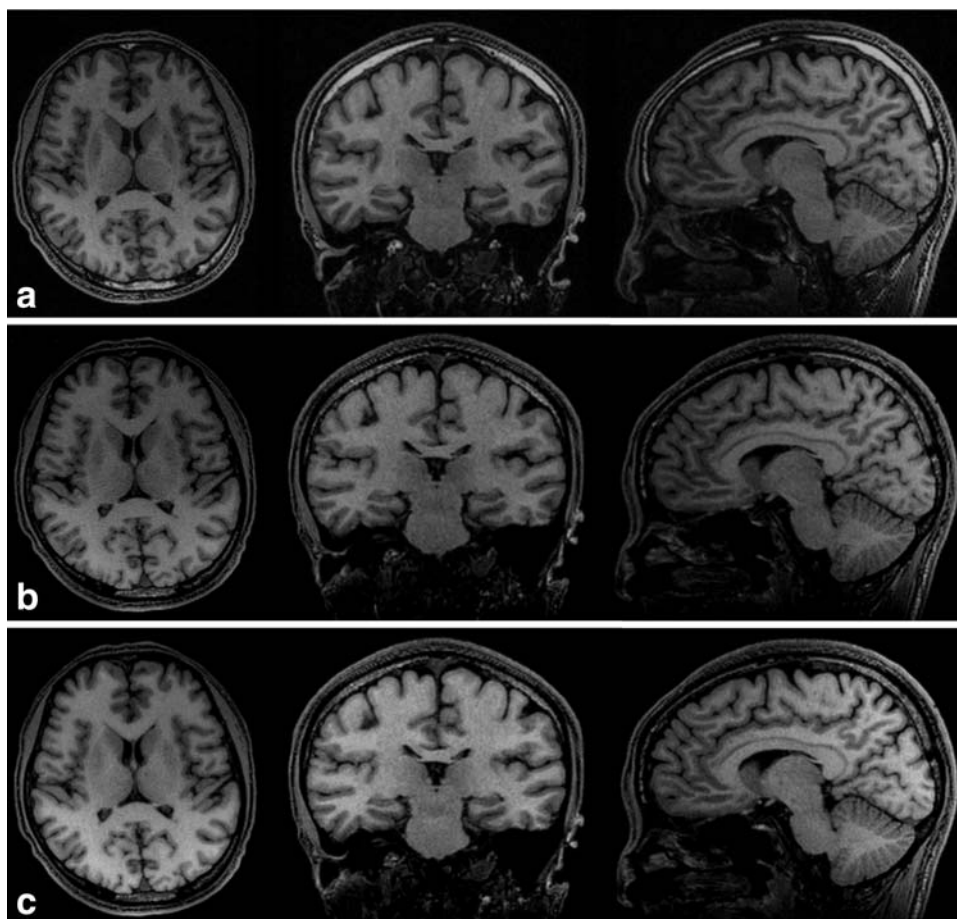


FIG. 7. IR-SPGR brain imaging. Representative axial, coronal, and sagittal images of the brain (zoomed-in) of a volunteer are shown for different schemes and readout trajectories. For scheme A, the concentric cylinder-based sequence (b) achieves higher SNR and similar CNR compared to the 3DFT sequence (a) while the total scan time was reduced by 63%. For scheme B with longer TI and TD, the concentric cylinder-based sequence (c) was able to achieve much higher SNR and CNR while it was still faster than the 3DFT-based sequence with scheme A (a). The SNR/CNR measurements are listed in Table 1.

k-space and less on the outer k-space compared to other schemes.

RESULTS

In vivo volunteer studies were conducted on a 1.5 T scanner (Signa Excite; GE Healthcare, Waukesha, WI) with maximum gradient amplitude of 40 mT/m and maximum slew rate of 150 mT/m/ms. Informed written consent approved by our institutional review board was obtained from all subjects prior to scanning.

IR-SPGR Brain Imaging

In vivo brain scans of two healthy volunteers were performed using an eight-channel head coil. The previously described schemes A (TI/TD = 600/0 ms) and B (TI/TD = 900/600 ms) were used with concentric cylinders, which were reconstructed with 3D gridding followed by zero-padding to achieve isotropic spatial resolution (0.55 mm). For scheme A, 3DFT with the same resolution and FOV was also compared as the readout trajectory with the following parameters: TE/TR = 2.5/7.0 ms, flip angle = 10° [parameters adapted from Wu et al. (22)], $T_{dummy} = 35$ ms (5 TRs), $T_{acqwnd} = 1008$ ms (144 TRs), readout bandwidth = ± 62.5 kHz ($8\mu\text{s/sample}$), 288 sampling points (2.30 ms), and $N_{seg} = 360$. The readout was in the R/L direction to minimize the number of phase encodings, and the phase

encodings were 1D centric-ordered in the A/P direction. The same zero-padding as concentric cylinders was used. Total scan time was 3 min 38 s (scheme A) and 5 min 24 s (scheme B) for concentric cylinders, whereas it was 9 min 56 s (scheme A) for 3DFT.

To quantitatively compare different schemes and readout trajectories, signal-to-noise ratio (SNR) and contrast-to-noise-ratio (CNR) measurements were performed on the manually selected regions of the reconstructed images. WM signal was measured from the homogeneous regions of the axial images, and GM signal was measured near the WM regions including the caudate nucleus (37). The noise standard deviation was estimated from the image background. The same regions were used for different schemes, and the measurements from two subjects were averaged.

Figure 7 shows representative axial, coronal, and sagittal images of the brain of a volunteer obtained with different schemes and readout trajectories. The corresponding SNR/CNR measurements are listed in Table 1. For scheme A, the concentric cylinder-based sequence (Fig. 7b) achieves higher SNR ($\text{SNR}_{WM} = 35.18$ vs. 31.41) and similar CNR ($\text{CNR}_{WM-GM} = 11.26$ vs. 11.63) compared to the 3DFT sequence (Fig. 7a) while the total scan time was reduced by 63%. For scheme B with longer TI and TD, the concentric cylinder-based sequence (Fig. 7c) achieves much higher SNR ($\text{SNR}_{WM} = 42.51$ vs. 31.41) and CNR ($\text{CNR}_{WM-GM} = 14.54$ vs. 11.63) while it was still almost 2-fold faster than the 3DFT sequence (Fig. 7a).

Table 1
SNR and CNR Measurements.

	Cylinders			3DFT Scheme A
	Scheme A		Scheme B	
Brain imaging ($n = 2$)				
Scan time:		3 min 38 s	5 min 24 s	9 min 56 s
SNR _{WM} :		35.18	42.51	31.41
SNR _{GM} :		23.92	27.97	19.78
CNR _{WM-GM} :		11.26	14.54	11.63
	Cylinders			3DFT Scheme III
	Scheme I	Scheme III-int	Scheme III-mix	
Peripheral angiography ($n = 4$)				
Scan time:	1 min 18 s	3 min 9 s	3 min 9 s	4 min 15 s
SNR _A :	32.94	30.94	24.81	26.40
SNR _V :	32.57	15.69	12.04	16.49
SNR _M :	10.05	10.03	6.84	7.17
SNR _F :	30.92	14.05	9.70	9.24
CNR _{A-V} :	0.37	15.25	12.77	9.91
CNR _{A-M} :	22.89	20.91	17.97	19.23
CNR _{A-F} :	2.02	16.89	15.11	17.16

Note: WM: white matter, GM: gray matter, A: artery, V: vein, M: muscle, F: fluid, n : number of subjects from which measurements were averaged.

NCE Magnetization-Prepared bSSFP Peripheral Angiography

To compare some of the different schemes of the proposed magnetization-prepared bSSFP sequence, in vivo lower extremity scans of four healthy volunteers were performed using a single-channel transmit-receive linear extremity coil. Three slabs were acquired to cover 12 cm in the S/I direction with two slices overlapped between adjacent slabs (32). For each slab, the sequence parameters were basically the same as those for the simulations shown in Figures 5 and 6. Images acquired with the concentric cylinders readout were reconstructed with 3D gridding followed by zero-padding to achieve isotropic spatial resolution (0.55 mm). For scheme III, 3DFT was also compared as the readout trajectory, where the same sequence parameters as the concentric cylinder-based sequence were used for each slab except for the following parameters: TE/TR = 2.6/6.2 ms, FOV = 14.1 × 31.7 × 5.3 cm³, 288 sampling points (1.15 ms), $N_{\text{seg}} = 48$, $T_{\text{prev}} = 102$ ms (40 ms + 10 TRs), $T_{\text{acqwnd}} = 396$ ms (64 TRs), and $T_{\text{post}} = 62$ ms (10 TRs). The readout was in the R/L direction to minimize the number of phase encodings, and the phase encodings were basically 1D centric-ordered in the A/P direction within each readout segment. For fluid, they were also centric-ordered in the S/I direction across the N_B readout segments following each block A. The same zero-padding as concentric cylinders was used. Total scan time was 1 min 18 s (scheme I) and 3 min 9 s (scheme III-int and scheme III-mix) for concentric cylinders, whereas it was 4 min 15 s (scheme III) for 3DFT.

To quantitatively compare different schemes and readout trajectories, SNR and CNR measurements were performed on the manually selected regions of the reconstructed images. Arterial signal was measured around the popliteal artery, anterior tibial artery, and posterior tibial artery. Also, venous signal from the deep vein and muscle/fluid signals

near the arterial regions were measured. The noise standard deviation was estimated from the image background. The same regions were used for different schemes, and the measurements from four subjects were averaged.

Figure 8 shows a coronal maximum-intensity-projection (MIP) image and two axial images of the right calf of a volunteer obtained with different schemes and readout trajectories. Compared to scheme I (Fig. 8a), scheme III-int (Fig. 8b) makes two noticeable improvements. First, arterial signal (arrow heads) is no longer obscured by fluid signal, which is well suppressed by the inversion preparation ahead of every $N_B = 6$ segment (dashed arrows). Second, artery-vein contrast is significantly improved by the venous saturation pulse ahead of every segment (solid arrows). These are quantitatively shown with SNR/CNR measurements in Table 1, where artery-vein and artery-fluid CNR of scheme III-int are significantly enhanced from 0.37 to 15.25 and 2.02 to 16.89, respectively. Scheme III-mix (Fig. 8c) further suppresses fluid signal, where the SNR (SNR_F) is reduced by 30% compared to scheme III-int. However, it also slightly increases fat signal (bone marrow in oval areas) and decreases arterial and muscle signals as expected from the simulation. Compared to the 3DFT sequence (Fig. 8d), the concentric cylinder-based sequence (schemes III-int and III-mix) on average achieves 40% higher artery-vein CNR while the total scan time was reduced by 25%.

To demonstrate the feasibility of the proposed parallel imaging method with concentric cylinders, another scan of both calves with scheme III-mix was performed using an eight-channel cardiac coil. Six slabs were acquired to cover 22 cm in the S/I direction. Other parameters were the same as those for the previous in vivo scans, which met the conditions of the proposed parallel imaging method. For each slab, the dataset was reformatted as 216 spoke-planes with matrix size 287 × 24. Then, it was retrospectively undersampled with a reduction factor $R = 2$. A GRAPPA-based reconstruction (38) was performed for each

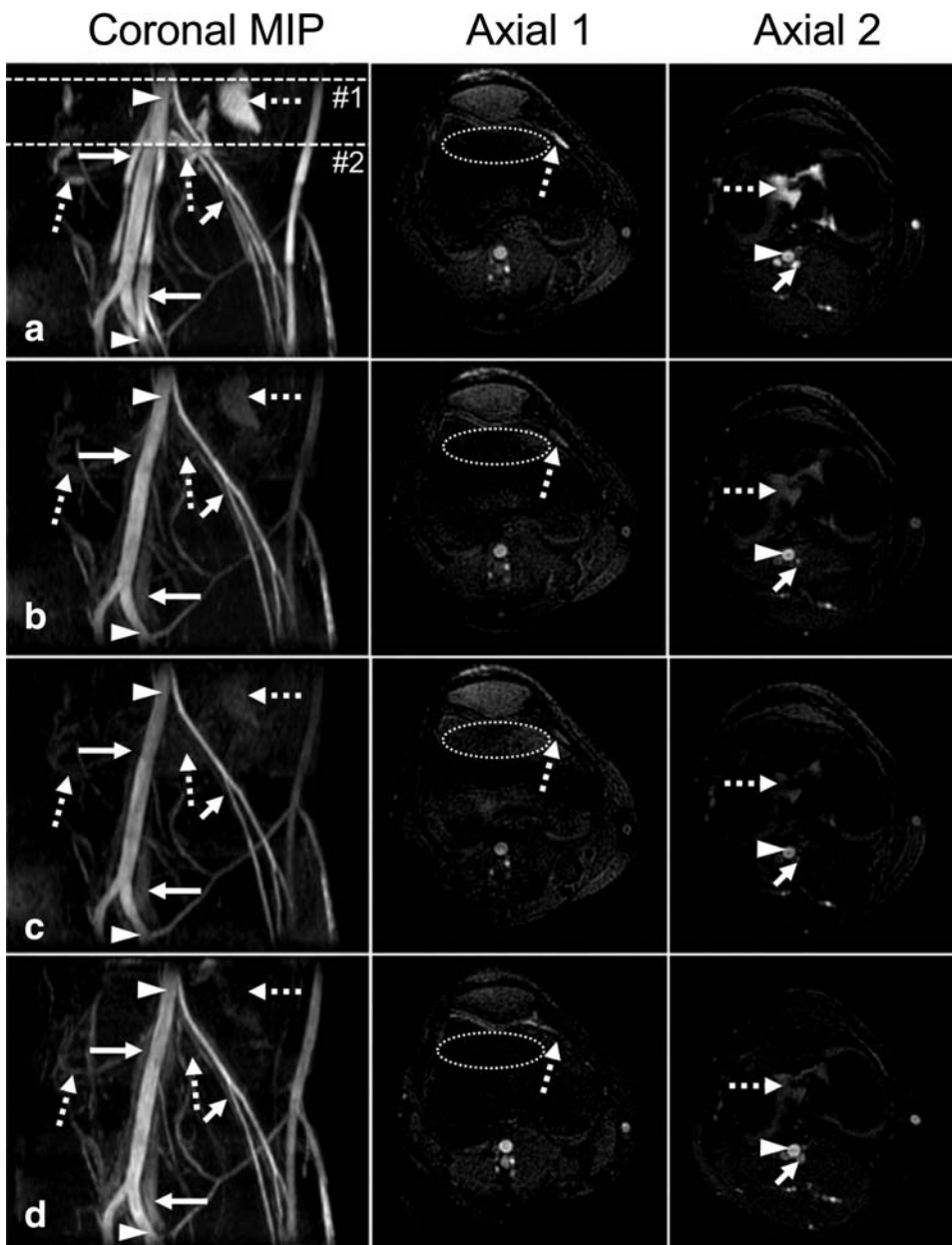


FIG. 8. NCE magnetization-prepared bSSFP peripheral angiography. A coronal MIP image (left) and two representative axial images (center and right) of the right calf (zoomed-in) of a volunteer are shown for different schemes (dashed lines: locations of axial slices) and readout trajectories. Concentric cylinders readout was used unless otherwise noted. Compared to scheme I (a), scheme III-int (b) provides better depiction of arterial signal (arrow heads) due to fluid (dashed arrows) and venous (solid arrows) suppression. The degree of fluid suppression is further improved with scheme III-mix (c), but it also slightly increases fat signal (bone marrow in oval areas) and decreases arterial and muscle signals. Compared to the 3DFT sequence (d), the concentric cylinder-based sequence in general achieves better artery-vein contrast. The SNR/CNR measurements are listed in Table 1.

spoke-plane with a fully sampled 35×24 autocalibration region from the inner 18 cylinders and a 5×5 interpolation kernel. Figure 9a shows the coronal MIP image of the calf with the proposed parallel imaging reconstruction, whose component axial slices (Fig. 9b and c) show comparable image quality to the fully sampled case other than the decrease of SNR. The original scan time (6 min 12 s) can be reduced to 56% (3 min 30 s) if the $R = 2$ undersampling pattern is used.

DISCUSSION

The 3D concentric cylinders trajectory is well-suited for magnetization-prepared imaging due to its unique properties. In addition to its robustness to off-resonance effects and timing delays (21,22), concentric cylinders

require a factor of $2N_{\text{rev}}$ fewer excitations than a comparable 3DFT sequence, which results in a scan-time reduction. In the brain scans with scheme A, the scan time of concentric cylinders was 37% of the 3DFT sequence when a similar T_{acqwind} was used, which was as expected with $N_{\text{rev}} = 3$ and different TRs used for each sequence (15.6 ms vs. 7.0 ms). The advantage in scan time can be traded off to facilitate the use of more imaging segments to better capture the contrast created by inversion recovery, or to enhance SNR and CNR by using longer TI and TD as in scheme B (22). The 3DFT sequence could have achieved improved SNR and CNR with a higher flip angle and rectangular/elliptical spiral of phase encodings (13), but the reduction in number of excitations afforded by concentric cylinders still allows more flexibility for magnetization-prepared imaging.

The proposed parallel imaging method for concentric cylinders reformats the 3D non-Cartesian data as a set of

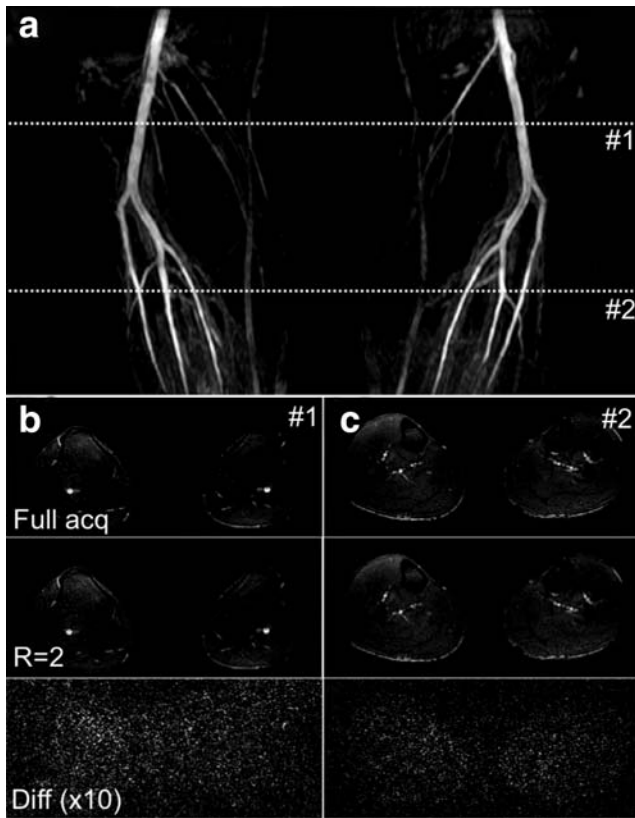


FIG. 9. Parallel imaging results with concentric cylinders. A coronal MIP image (a) and two representative axial images (b, c) are shown, which were retrospectively undersampled with a reduction factor $R = 2$ and reconstructed by the proposed parallel imaging method (dashed lines: locations of axial slices). Each component axial slice shows comparable image quality to the fully sampled case other than the decrease of SNR.

2D Cartesian spoke-planes that cross the center of k -space. With this distinct sampling geometry, a k -space-based 2D Cartesian parallel imaging reconstruction can be independently applied to each spoke-plane, which can be solved much faster than considering the entire 3D non-Cartesian data together. This can facilitate the use of concentric cylinders with more efficiency for magnetization-prepared imaging, and an initial in vivo result with this method (Fig. 9) showed comparable image quality to the fully sampled case. Although this method enables a faster reconstruction, the azimuthal neighbors on multiple spoke-planes are not used to estimate the missing data. A detailed comparison between this method and a fully 3D non-Cartesian parallel imaging reconstruction for different reduction factors would be very beneficial.

The inherently centric-ordered structure of concentric cylinders in the k_x and k_y dimensions is ideal for effectively capturing the transient magnetization-prepared contrast. In the lower extremity scans, better venous suppression was achieved in the sequence with concentric cylinders than 3DFT, although both sequences were based on the same preparation scheme (scheme III) and similar acquisition windows. The difference was mainly due to the fact that the concentric cylinders readout captured the low

spatial frequency components of the suppressed venous signal both in the A/P and R/L directions, whereas the 1D centric-ordered 3DFT readout captured them only in the A/P direction. A rectangular/elliptical spiral of phase encodings (13) may help achieve more effective venous suppression for 3DFT, but the view ordering needs to be more carefully designed to avoid any undesirable fluctuation of k -space weighting that might result from the periodic variation of fluid signal evolution in scheme III.

In the lower extremity scans, the degree of fluid suppression generally followed the trends in the simulation, where scheme III-mix achieved the best fluid suppression other than scheme II among cylinders. However, it ended up with lower overall CNRs than scheme III-int (15.11 vs. 16.89) due to the decrease of arterial signal. In this sense, scheme III-int would be chosen over scheme III-mix, but the level of sidelobes (Fig. 6) also needs to be considered, particularly when fluid has a diffuse distribution in the volume of interest (e.g., foot).

The fluid suppression with scheme III-mix was not as good as the simulated level for some regions. This might be due to the fact the actual distribution of fluid was not as isotropic as the sphere phantom used in the simulation, which led to an anisotropic k -space pattern in 3D. For example, the distribution of fluid indicated with the horizontal dashed arrows in Figure 8 was quite limited in the A/P and R/L directions, which might not have much low spatial frequency components to suppress from the start. This could also explain why the 3DFT sequence achieved better fluid suppression for that region. That is, it might have more low spatial frequency components in the S/I direction than other two directions, where the S/I direction was actually a centric-ordered dimension of the 3DFT sequence for fluid. To avoid this kind of dependency, trajectories that can be centric-ordered in all 3D (22) need to be used.

There are several possible improvements to the concentric cylinder-based magnetization-prepared sequence. First, it could be implemented as a partial-echo sequence to reduce the echo time and any potential flow artifacts. This is relatively straightforward to implement compared to other non-Cartesian trajectories due to the constant G_z gradient. Second, a multiband version of cylinders could be implemented to reduce the scan time (39), with an extra step in the reconstruction to correct the different amount of bulk rotation of each band due to timing delays. Third, specifically for the angiography application, a sliding interleaved k_y (SLINKY) (40) version of concentric cylinders may reduce venetian-blind artifacts and distribute the venous-suppression effects more evenly over the FOV (41). For example, the bottom half of Figure 9a with incomplete venous-suppression effects, possibly due to slow venous flow and/or system imperfection such as B_1 -field inhomogeneity, could be improved. Finally, the scan time could be further reduced by a variable-density sampling version of concentric cylinders (42).

CONCLUSIONS

We have demonstrated that the 3D concentric cylinders trajectory is an efficient readout for magnetization-prepared imaging. In addition to the inherently centric-ordered

structure, concentric cylinders do not require off-resonance and timing delay corrections while fewer excitations are required than a comparable 3DFT sequence. Also, a tailored interleaving scheme and an efficient parallel imaging method can be applied. IR-SPGR T_1 -weighted brain imaging and NCE magnetization-prepared bSSFP peripheral angiography have been presented as potential applications that benefit from the 3D concentric cylinders trajectory.

ACKNOWLEDGMENT

The authors thank Nii Okai Addy for helpful discussions about non-Cartesian trajectories and providing a framework for online non-Cartesian reconstruction.

REFERENCES

- Mugler JP III, Brookeman JR. Rapid three-dimensional T_1 -weighted MR imaging with the MP-RAGE sequence. *J Magn Reson Imaging* 1991;1:561–567.
- Lin C, Bernstein MA. 3D magnetization prepared elliptical centric fast gradient echo imaging. *Magn Reson Med* 2008;59:434–439.
- Stöcker T, Shah NJ. MP-SAGE: A new MP-RAGE sequence with enhanced SNR and CNR for brain imaging utilizing square-spiral phase encoding and variable flip angles. *Magn Reson Med* 2006;56:824–834.
- Deichmann R, Good CD, Josephs O, Ashburner J, Turner R. Optimization of 3-D MP-RAGE sequences for structural brain imaging. *NeuroImage* 2000;12:112–127.
- Brittain JH, Hu BS, Wright GA, Meyer CH, Macovski A, Nishimura DG. Coronary angiography with magnetization-prepared T2 contrast. *Magn Reson Med* 1995;33:689–696.
- Deshpande VS, Shea SM, Laub G, Simonetti OP, Finn JP, Li D. 3D magnetization-prepared true-FISP: a new technique for imaging coronary arteries. *Magn Reson Med* 2001;46:494–502.
- Scheffler K, Heid O, Hennig J. Magnetization preparation during the steady state: fat-saturated 3D trueFISP. *Magn Reson Med* 2001;45:1075–1080.
- Richardson DB, Bampton AE, Riederer SJ, MacFall JR. Magnetization-prepared MR angiography with fat suppression and venous saturation. *J Magn Reson Imaging* 1992;2:653–664.
- Holsinger AE, Riederer SJ. The importance of phase-encoding order in ultra-short TR snapshot MR imaging. *Magn Reson Med* 1991;16:481–488.
- Wilman AH, Rossman J, King F, Debbins JP, Rossman PJ, Ehman RL. Fluoroscopically triggered contrast-enhanced three-dimensional MR angiography with elliptical centric view order: application to the renal arteries. *Radiology* 1997;205:137–146.
- Wielopolski PA, Manning WJ, Edelman RR. Single breath-hold volumetric imaging of the heart using 3-dimensional segmented echo planar imaging. *J Magn Reson Imaging* 1995;4:403–409.
- Wang Y, Rossman PJ, Grimm RC, Wilman A H, Riederer SJ, Ehman RL. 3D MR angiography of pulmonary arteries using real-time navigator gating and magnetization preparation. *Magn Reson Med* 1996;36:579–587.
- Wilman AH, Riederer SJ. Improved centric phase encoding orders for three-dimensional magnetization-prepared MR angiography. *Magn Reson Med* 1996;36:384–392.
- Nugent AC, Johnson GA. T1rho imaging using magnetization-prepared projection encoding (MaPPE). *Magn Reson Med* 2000;43:421–428.
- Foltz WD, Chopra S, Chung P, Bayley A, Catton C, Jaffray D, Wright GA, Haider MA, Ménard C. Clinical prostate T2 quantification using magnetization-prepared spiral imaging. *Magn Reson Med* 2010;64:1155–1161.
- Shu Y, Riederer SJ, Bernstein MA. Three-dimensional MRI with an undersampled spherical shells trajectory. *Magn Reson Med* 2006;56:553–562.
- Wong EC. Magnetic resonance functional neuroimaging using interleaved SUNBURST. In *Proceeding of the 2nd Annual Meeting of SMR*, San Francisco, California, USA, 1994. p. 25.
- Mugler JP III. Three-dimensional spin-echo imaging using cylindrical k-space trajectories. In *Proceedings of 3rd Annual Meeting of SMR*, Nice, France, 1995. p. 483.
- Ruppert K, Mugler JP III. Implementation of a 3D interleaved-cylindrical spin-echo sequence. In *Proceedings of the 7th Annual Meeting of ISMRM*, Philadelphia, Pennsylvania, USA, 1999. p. 1630.
- Ruppert K, Mugler J P III. 3D hyperpolarized ^3He MR imaging of the lung using an interleaved-cylindrical k-space trajectory. In *Proceedings of the 9th Annual Meeting of ISMRM*, Glasgow, Scotland, UK, 2001. p. 945.
- Ruppert K, Oshio K, Guenther M, Mugler JP III. An interleaved cylindrical k-space trajectory for rapid 3D GRE acquisitions. In *Proceedings of the 11th Annual Meeting of ISMRM*, Toronto, Canada, 2003. p. 208.
- Wu HH, Nishimura DG. 3D magnetization-prepared imaging using a stack-of-rings trajectory. *Magn Reson Med* 2010;63:1210–1218.
- Wu HH, Lee J H, Nishimura DG. MRI using a concentric rings trajectory. *Magn Reson Med* 2008;59:102–112.
- Wu HH, Lustig M, Nishimura DG. Parallel imaging using a 3D stack-of-rings trajectory. In *Proceedings of the Joint Annual Meeting ISMRM-ESMRMB*, Stockholm, Sweden, 2010. p. 2878.
- Silver MS, Joseph RI, Hoult DI. Highly selective $\pi/2$ and π pulse generation. *J Magn Reson* 1984;59:347–351.
- Brittain JH, Shimakawa A, Wright GA, Hargreaves BA, Han E, Stainsby JA, Hu B. Non-contrast-enhanced, flow-independent, 3D peripheral angiography using steady-state free precession at 3T. In *Proceedings of the 11th Annual Meeting of ISMRM*, Toronto, Canada, 2003. p. 1710.
- Stafford RB, Sabati M, Mahallati H, Frayne R. 3D non-contrast-enhanced MR angiography with balanced steady-state free precession Dixon method. *Magn Reson Med* 2008; 59: 430–433.
- Çukur T, Shimakawa A, Yu H, Hargreaves Ba, Hu BS, Nishimura DG, Brittain JH. Magnetization-prepared IDEAL bSSFP: a flow-independent technique for noncontrast-enhanced peripheral angiography. *J Magn Reson Imaging* 2011;33:931–939.
- Spincemaille P, Nguyen TD, Wang Y. View ordering for magnetization prepared steady state free precession acquisition: application in contrast-enhanced MR angiography. *Magn Reson Med* 2004;52:461–466.
- Bieri O, Markl M, Scheffler K. Analysis and compensation of eddy currents in balanced SSFP. *Magn Reson Med* 2005;54:129–137.
- Nezafat R, Ouwerkerk R, Derbyshire AJ, Stuber M, McVeigh ER. Spectrally selective B1-insensitive T2 magnetization preparation sequence. *Magn Reson Med* 2009;61:1326–1335.
- Parker DL, Yuan C, Blatter DD. MR angiography by multiple thin slab 3D acquisition. *Magn Reson Med* 1991;17:434–451.
- Gold GE, Han E, Stainsby J, Wright GA, Brittain JH, Beaulieu CF. Musculoskeletal MRI at 3.0 T: relaxation times and image contrast. *AJR Am J Roentgenol* 2004;183:343–351.
- Wright GA, Nishimura DG, Macovski A. Flow-independent magnetic resonance projection angiography. *Magn Reson Med* 1991;17:126–140.
- Dharmakumar R, Hong J, Brittain JH, Plewes DB, Wright GA. Oxygen-sensitive contrast in blood for steady-state free precession imaging. *Magn Reson Med* 2005;53:574–583.
- Koay CG, Sarlls JE, Özarslan E. Three-dimensional analytical magnetic resonance imaging phantom in the Fourier domain. *Magn Reson Med* 2007;58:430–436.
- Epstein FH, Mugler III JP, Brookeman JR. Optimization of parameter values for complex pulse sequences by simulated annealing: application to 3D MP-RAGE imaging of the brain. *Magn Reson Med* 1994;31:164–177.
- Griswold MA, Jakob PM, Heidemann RM, Nittka M, Jellus V, Wang J, Kiefer B, Haase A. Generalized autocalibrating partially parallel acquisitions (GRAPPA). *Magn Reson Med* 2002;47:1202–1210.
- Ruppert K, Mugler III JP. An optimized 3D interleaved cylindrical pulse sequence with reduced oversampling. In *Proceedings of the 12th Annual Meeting of ISMRM*, Kyoto, Japan, 2004. p. 2112.
- Liu K, Rutt BK. Sliding interleaved ky (SLINKY) acquisition: a novel 3D MRA technique with suppressed slab boundary artifact. *J Magn Reson Imaging* 1998;8:903–911.
- Brittain JH, Pauly JM, Kerr AB, Nishimura DG. SLINKY MRA with time-varying gradients and flow-independent contrast. In *Proceedings of the 7th Annual Meeting of ISMRM*, Philadelphia, Pennsylvania, USA, 1999. p. 1913.
- Tsai CM, Nishimura DG. Reduced aliasing artifacts using variable-density k-space sampling trajectories. *Magn Reson Med* 2000;43:452–458.